Observation of orbital selective charge transfer in a Fe/$BaTiO_3$ interfacial two-dimensional electron gas

Byungmin Sohn,[1,2,*,†] Guillaume Marcaud,[1,*] Yeongjae Shin,[1] Sangjae Lee,[3] Tyler Werner,[1] Turgut Yilmaz,[4] Jinming Yang,[3] Wenzheng Wei,[1] Alexei Fedorov,[5] Elio Vescovo,[4] Yu He,[1] Sohrab Ismail-Beigi,[1] Charles H. Ahn,[1,3,‡] and Frederick J. Walker[1,§]

[1]*Department of Applied Physics, Yale University, New Haven, Connecticut 06520, USA*
[2]*Department of Physics, Sungkyunkwan University, Suwon 16419, Korea*
[3]*Department of Physics, Yale University, New Haven, Connecticut 06520, USA*
[4]*National Synchrotron Light Source II, Brookhaven National Laboratory, Upton 11973, New York, USA*
[5]*Advanced Light Source, Lawrence Berkeley National Laboratory, Berkeley, California 94720, USA*

(Received 12 April 2023; revised 14 March 2024; accepted 15 March 2024; published 2 April 2024)

Two-dimensional electron gas (2DEG) states at oxide interfaces between two ferroic materials have been fertile ground to realize controllable multiferroicity. Here, we investigate the 2DEG states at the interface of ferroelectric $BaTiO_3$ and a magnetic layer of iron using angle-resolved photoemission spectroscopy. Orbital-selective charge transfer occurs on the surprisingly robust 2DEG. Based on first-principles calculations, we show how the interfacial hybridization can give rise to the unexpected charge transfer in the magnetic 2DEG. Our study reveals a close interplay on a 2DEG between magnetic and ferroelectric interfaces, which sheds light on future design principles of multiferroic 2DEG states.

DOI: 10.1103/PhysRevB.109.155106

Realizing spin electronics (spintronics) by controlling spin and charge degrees of freedom has been intensively studied for decades [1,2]. Multiferroicity, where two or more ferroic orders such as ferroelectricity, ferromagnetism, and ferroelasticity are exhibited simultaneously, has been of keen interest as one of the candidates for promising spintronic devices [3,4]. In particular, magnetoelectric multiferroic materials where ferroelectricity and ferromagnetism coexist have been of great interest for future device applications due to the possibility of reduced power for switching the device state [3–5]. However, due to the contradictory requirement of multiferroicity in d-band transition metal oxides—that is, ferroelectricity is favored by d^0 transition metal ions, whereas ferromagnetism is preferred in partially filled d (or f) shells [6,7]—relatively few single-phase multiferroic materials have been reported [8–10]. Moreover, the empty d orbital state makes multiferroic materials prefer insulating ground states, which makes it challenging to utilize multiferroicity for current-controlled electronic devices.

One solution is to design heterogeneous interfaces consisting of both ferromagnetic and ferroelectric materials to realize interfacial multiferroicity [11–15]. In addition, several ferroelectric/metallic-ferromagnetic oxide interfaces such as $BaTiO_3$/Fe [16–18] and (La,Sr)MnO_3/$BaTiO_3$ [19,20] have been proposed to address the lack of electrical conductivity in multiferroic systems. These heterostructures are often susceptible to forming two-dimensional electron gas (2DEG) states, which can have high carrier mobility [21–23], can be tuned under electric/magnetic fields [5,24], and can operate sustainably in atmospheric conditions [25]. As a result, many spintronic devices have been conceived based on oxide heterostructures with ferroic 2DEG states [5,26,27], including a recent report on Ca-$SrTiO_3$/$EuTiO_3$/$LaAlO_3$ heterostructures [28].

However, in magnetic metal/ferroelectric oxide heterostructures, interfacial charge transfer is an essential variable that can substantially alter the original magnetic and ferroelectric orders. Of particular importance, interfacial oxygen diffusion effects have not been well studied in this context, where the metallic layer tends to extract oxygen atoms from the ferroelectric side. It remains unclear how the charge transfer and bonding across such interfaces will occur across the interface. Therefore, investigating directly the electronic and magnetic structures of such interfaces is crucial [29–31] to understand exotic interface-driven phenomena such as multiferroic 2DEG [28]. Especially for tunnel devices, the detailed electronic structure plays a determinant role in the tunnel probability and the macroscopic behavior of the tunnel process through the Landauer-Buttiker formula [19]. Here, we measure these electronic structure details by fabricating a monolayer-thick Fe magnetic layer on oxide ferroelectric thin films of $BaTiO_3$ (BTO) [Fig. 1(a)] and perform *in situ* investigations of the electronic structure of the 2DEG with angle-resolved photoemission spectroscopy (ARPES). Combining experimental and theoretical investigations, we report a nontrivial charge transfer in the 2DEG due to atomic bonding on the interface. Our study clarifies how the electronic structures are influenced by the interfacial interactions at ferroic oxide interfaces.

*These authors contributed equally to this work.
†byungmin.sohn@yale.edu
‡charles.ahn@yale.edu
§fred.walker@yale.edu

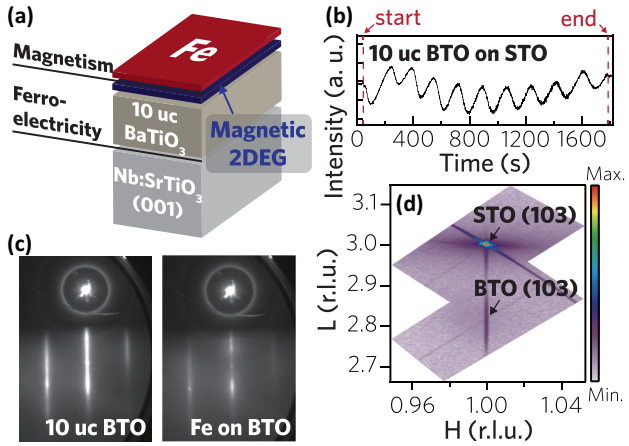

FIG. 1. Structure of interface-induced magnetic two-dimensional electron gas (2DEG). (a) A schematic of the interface between a magnetic layer of Fe and a ferroelectric layer of 10-unit-cell (uc) $BaTiO_3$ (BTO). (b) Reflection high-energy electron diffraction (RHEED) intensity plot during the growth of a 10-uc BTO film. (c) RHEED patterns along the $[11]_{pc}$ direction before and after depositing Fe atoms on a 10-uc BTO film. (d) Reciprocal space mapping of a 10-uc BTO film.

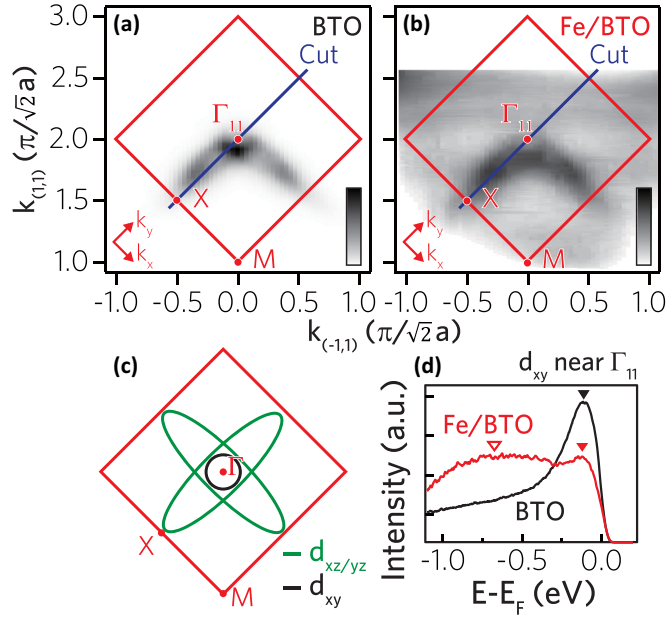

FIG. 2. Robust 2DEG prior to and after Fe deposition. (a), (b) Fermi surfaces of 2DEG in BTO and Fe/BTO films. Red squares represent the Brillouin zone boundary. (c) Schematic of the Fermi surface of the 2DEG. A black (green) solid line indicates a d_{xy} ($d_{xz/yz}$) band. (d) Energy distribution curves of 2DEG in BTO (black) and Fe/BTO (red) films at $(k_{(-1,1)}, k_{(1,1)}) = (0, 1.9)$. Filled inverted triangles indicate coherent peaks near E_F. After Fe deposition, incoherent spectral weight appears around $E = E_F - 0.7$eV (open-inverted triangle).

To study the 2DEG states between magnetic and ferroelectric layers, two thin films have been prepared: 10-unit-cell (uc) BTO thin films on Nb-doped $SrTiO_3$ (STO) (001) are prepared, and capped with 1.74 monolayer (ML) of Fe deposited at 60 °C in vacuum (1 ML $= 6.578 \times 10^{14}$ atoms/cm^2 $= 1$ atom/ (3.905 Å)^2, the area of a $SrTiO_3$ surface mesh). Hereinafter, we denote the two types of samples as BTO and Fe/BTO. Figure 1(b) shows a reflection high-energy electron diffraction (RHEED) intensity plot for the BTO film. RHEED patterns are observed during the growth and remain unchanged after Fe atoms are deposited [Fig. 1(c)]. The observed diffraction is consistent with the epitaxial growth of Fe_2O_2 on the BTO with an orientation and structure shown in Fig. 4(a), used for the first principles modeling, and observed in scanning transmission electron microscopy for thicker Fe/BTO interfaces prepared in a manner similar to that used here [32]. Figure 1(d) shows reciprocal space mapping measured on the BTO thin film. The BTO film is fully strained to the STO substrate below it, and the difference in the out-of-plane lattice constants is 6.3% ($c = 4.151$Å) and consistent with elastically strained bulk tetragonal BTO, which gives 4.13 Å (See Sec. V of the Supplemental Material for discussion [33]). The c-axis lattice constant of our film is almost the same as that of the reported 7-nm BTO film on an STO substrate, $c_{BTO} = 4.16$ Å [52], larger than for BTO/STO superlattices grown on STO $c_{BTO} = 4.04$ Å [53], and smaller than a $SrRuO_3/BaTiO_3/SrRuO_3$ structure where $c_{BTO} = 4.21$ Å [54].

To measure the electronic structure of the 2DEG, we perform ARPES on the BTO and Fe/BTO films and compare the resulting spectra [Figs. 2(a) and 2(b)]. Figure 2(c) shows a schematic of the Fermi surface of the ultraviolet light (UV) induced 2DEG states. Note that the schematic of the Fermi surface has been examined by conducting ARPES with different photon polarizations (see Fig. S1 for the discussion about the schematic [33]). An electron pocket marked with a black solid line near the Γ point consists of Ti $3d_{xy}$ orbitals, whereas two ellipsoidal electron pockets elongated along the Γ-X direction (marked with a green solid line) consist mainly of Ti $3d_{xz}$ and $3d_{yz}$ orbitals [51]. For compactness, we denote Ti $3d_{xy}$, $3d_{yz}$, and $3d_{xz}$ orbitals as d_{xy}, d_{yz}, and d_{xz}, respectively. Figures 2(a) and 2(b) show the measured Fermi surfaces of the 2DEG states for BTO and Fe/BTO. Both bare BTO and Fe/BTO surfaces are exposed to UV irradiation of 150-eV photons for more than an hour until the pocket sizes stabilize, which is due to the formation of a sufficient number of oxygen vacancies under UV irradiation [55].

Figure 2(d) shows energy distribution curves (EDCs) of the d_{xy} band near the Γ_{11} point. We observe coherent quasiparticle peaks in both samples indicated by filled inverted triangles. In Fe/BTO, an incoherent spectral hump appears in the high-binding energy region ($-1\,\text{eV} < E - E_F < -0.3\,\text{eV}$, where E_F is the Fermi level), highlighted by an open inverted triangle. Since the coherent quasiparticle peaks remain sharply defined in momentum space, the incoherent spectrum is unlikely from simple elastic impurity scattering of the 2DEG electrons [56]. We have found that Fe is oxidized in Fe/BTO by performing core-level photoemission spectroscopy (PES) [see Fig. S2(a) [33]].

To compare the band structures of the two systems, we plot in Figs. 3(a) and 3(b) energy-momentum (E-k) slices of the spectra along the Γ_{11}-X direction [solid blue lines in Figs. 2(a) and 2(b)]. Two electronlike pockets (d_{xy} and d_{xz}) are observed in both E-k cuts. Momentum distribution

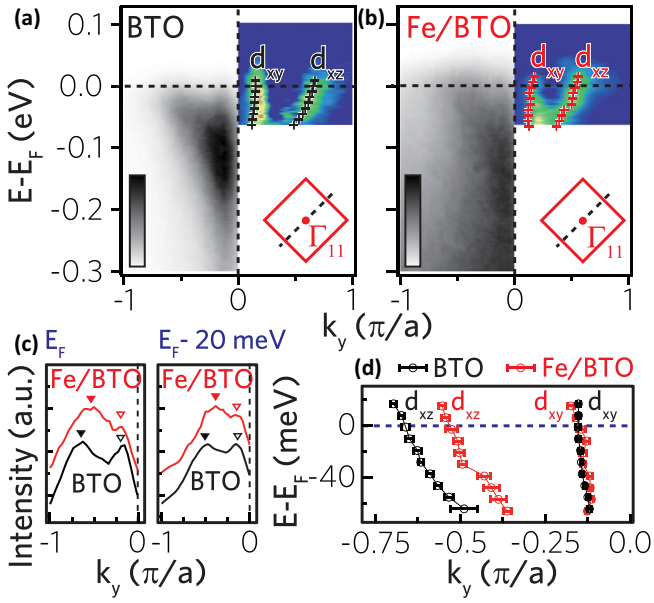

FIG. 3. Fe-induced, orbital-selective charge transfer at the interface. (a), (b) *E-k* dispersion of BTO and Fe/BTO films along the k_y direction. Here, we define k_y at Γ_{11} as zero. 2D curvature band dispersions [60] and fit results with a Lorentzian function are plotted on right. (c) Momentum distribution curves (MDCs) at the Fermi level (E_F) and $E_F - 20$ meV. Open (closed) inverted triangles represent peaks for the d_{xy} (d_{xz}) bands. (d) Peak positions of d_{yz} and d_{xy} bands of BTO and Fe/BTO films. Black (red) open circles represent data from BTO (Fe/BTO) film.

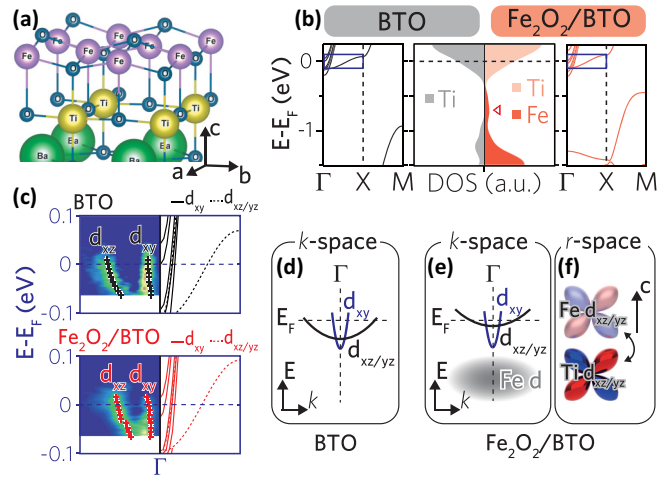

FIG. 4. *Ab initio* results for the Fe_2O_2/BTO interface. (a) Geometry of the monolayer Fe_2O_2/BTO heterostructure. (b) *Ab initio* calculated band structures and density of states (DOS) of (left) BTO and (right) Fe_2O_2/BTO films. Atom-projected DOS of the BTO (Fe_2O_2/BTO) film is plotted at the center with black (red) depending on the type of atom. A red open triangle is placed at $E = E_F - 0.7$ eV. (c) (left) Enlarged 2D curvature band dispersions with fit results [adapted from Figs. 3(a) and 3(b)] and (right) calculated *E-k* dispersions for bands with mainly Ti 3*d* orbital character. The enlarged regions are represented with blue rectangles in (b). (d)–(f) Schematic band structures and atomic orbital interaction in (d) BTO and (e),(f) Fe_2O_2/BTO films. The double-ended arrows represent electron hopping between orbitals.

curves (MDCs) at E_F [Fig. 3(c)] show two peaks in each cut, where the peaks from the d_{xz} (d_{xy}) orbital are marked with closed (open) inverted triangles. Fitted 2DEG band dispersions before and after Fe deposition are shown in the insets of Figs. 3(a) and 3(b). To compare the difference in detail, Fig. 3(d) shows the peak positions of the d_{xz} and d_{xy} bands versus momentum. The peak positions of the d_{xz} band change with Fe deposition, and its Fermi momentum k_F changes from -0.53 to -0.42 Å^1, corresponding to an estimated change in carrier density from 8.3×10^{13} to 6.6×10^{13} cm^{-2}. On the other hand, the peak positions of the d_{xy} orbital remain at the same position with $k_F \pm 0.02$ Å^{-1} corresponding to a carrier density of 7.7×10^{12} cm^{-2}. Similar analysis along the Γ_{11}-*M* direction also shows little change in the d_{xy} pocket size (Fig. S3 [33]). This defies the natural expectation of Fe 4*s* electrons being completely ionized and filling the low-energy Ti 3*d* bands near E_F. As a result, the Fe on the ferroelectric surface induces an unconventional orbital-selective charge transfer in the 2DEG state.

Direct structural characterization of such a monolayer metal-oxide interface is challenging given the necessity to maintain an *in situ* environment to prevent extrinsic oxidization, especially when possible interfacial oxygen diffusion is part of the investigation. To decipher the property of the interface, we combine *in situ* surface electronic and structural characterizations with *ab initio* calculations of a comprehensive set of possible surface configurations. First, the RHEED patterns of the Fe/BTO film suggest that Fe grows as a flat single-crystalline monolayer on the BTO surface [Fig. 1(c)]. The iron flux administered during the *in situ* synthesis corresponds to approximately two irons per primitive BTO surface unit cell (see the Methods section in the Supplemental Material [33]). Meanwhile, core-level PES results [Fig. S2(a) [33]] suggest oxidized Fe with a predominately and Fe^{2+} oxidation state, consistent with Fe_2O_2 (see Sec. IV in the Supplemental Material [33]) [57]. To further understand the interfacial composition and structure, it is useful to perform *ab initio* calculations on a large number of surface structures where we consider either one or two Fe atoms per surface unit cell along with zero, one, or two added oxygen atoms. Multiple initial guesses for the initial starting geometry are used for structural relaxations, and a range of Fe 3*d* and Ti 3*d* *U* values (within DFT + *U* theory) are used along with ferromagnetic and antiferromagnetic Fe magnetic moment alignments.

After identifying the ground state lattice structure for each composition, we compute the electronic band structures for structure screening. The correct interface structure should obey two qualitative APRES observations: (i) after Fe deposition, there are no additional bands crossing the Fermi energy (e.g., Fe 4*s* or 3*d* bands); (ii) both d_{xz}/d_{yz} and d_{xy} Ti 3*d* bands are present at the Fermi energy before and after Fe deposition. We find that only the Fe_2O_2 composition with Fe 3*d* $U \geqslant 3$ eV obeys both conditions. The structure for $U = 3$ eV is shown in Fig. 4(a): the Fe_2O_2 layer has a buckled rocksalt structure, both Fe atoms are bonded to the O atoms of the TiO_2 layer below, a lower buckled O is bonded to the Ti below, while the upper buckled O is above a void site of the TiO_2 layer. This particular structure for $U = 3$ eV has an antiferromagnetic

ground state, but a competing ferromagnetic state may still be stabilized by fine-tuning the Fe U value. Regarding the oxygen content, we find that O has a strong energetic preference to oxidize the initially metallic Fe even under the high-vacuum conditions in the experiment (see Sec. III in the Supplemental Material [33]).

Taken in totality, we conclude that when Fe is deposited on the BTO surface, the resulting interface is Fe_2O_2/BTO rather than the prevalently discussed Fe/BTO. This is also consistent with the observation of the lack of large charge transfer from Fe 4s to Ti 3d. The *ab initio* calculated band structures of BTO and Fe_2O_2/BTO films are compared in Fig. 4(b). Both show 2DEG bands with Ti 3d orbital components at and near E_F, suggesting the Fe_2O_2 layer is not responsible for 2DEG states. On the other hand, the Fe_2O_2/BTO film additionally displays band dispersions from Fe 3d orbitals in the range $E_F - 0.5$ eV to $E_F - 1.5$ eV. Our calculated density of states (DOS) shows the Fe-induced states [center panel of Fig. 4(b)], which are marked with a red open triangle at $E = E_F - 0.7$eV. This result is consistent with our experimental observation of the peak of the incoherent spectral weight near the same energy [Fig. 2(d)]. The *ab initio* results are also supported by Fe-resonant ARPES data (Fig. S2 [33]), which show a strong enhancement of Fe spectral weight at high binding energy and suppression of Ti 3d weight.

We now turn to the low-energy electronic structure of this system. As shown in Fig. 3, the out-of-plane d_{xz} band is lifted in energy and subsequently loses charge, whereas the in-plane (d_{xy}) bands are almost unchanged in energy or occupancy. Such an orbital-selective charge transfer in Ti t_{2g} bands is reproduced in our *ab initio* calculation and is compared to experimental results in Fig. 4(c). Analysis of the first principles electronic structure tells us the microscopic mechanism of such an orbital-selective charge transfer, as illustrated in Figs. 4(d) and 4(e), is due to Ti-Fe hybridization [12,32,58,59]. We start with the bare BTO surface with a 2DEG having in-plane d_{xy} and out-of-plane $d_{xz/yz}$ bands. When the Fe_2O_2 layer is placed on the BTO surface, the wave functions of the in-plane Ti d_{xy} bands barely couple to the overlayer and are thus essentially unperturbed, while the wave functions for the out-of-plane $d_{xz/yz}$ bands hybridize with the out-of-plane Fe 3d bands. As the Fe 3d bands are mainly below E_F (and thus below the Ti $d_{xz/yz}$ bands), the hybridization leads to upward level repulsion pushing the Ti $d_{xz/yz}$ bands up in energy and selectively depopulating them.

Future experiments that build on this work include in-plane magnetotransport measurements to verify both the conducting nature of the 2DEG and its carrier density, and field effect measurements of the 2DEG through the application of a voltage on the Nb:STO substrate to flip the ferroelectric polarization and modulate the in-plane transport [13]. The devices required for this work will involve architectures that generate and maintain the 2DEG during fabrication and measurement. For example, capping layers are needed to protect the oxygen vacancies responsible for the 2DEG [51]. Ultimately, one may test whether such an interface, especially with the surprisingly robust 2DEG and iron local moments, becomes truly multiferroic.

In conclusion, we investigate interfacial 2DEG states emergent at a magnetic and ferroelectric interface with ARPES measurements. A single magnetic layer on a ferroelectric thin film induces orbital-dependent charge transfer in out-of-plane Ti $3d_{xz/yz}$ bands while the in-plane Ti $3d_{xy}$ bands remain the same. Our *ab initio* calculations show that the anisotropic hybridization between Fe and Ti 3d orbitals across the interface leads to orbital-dependent charge transfer. Our results indicate a possibility to perform orbital specific engineering at an interface, which may help increase spin polarization for potential device applications.

We gratefully acknowledge discussions with Y. Kim. This work was supported by the Air Force Office of Scientific Research (AFOSR) under Grant No. FA9550-21-1-0173. Work at beamline 21-ID-1 at NSLS II was supported by U.S. DOE Office of Science operated by Brookhaven National Laboratory under Contract No. DE-SC0012704 and by a BNL-Yale partner user agreement. S.I.B. and Y.H. acknowledge partial salary support from the National Science Foundation (NSF) via EAGER Grant No. DMR 2132343. S.I.B. also thanks the Yale Center for Research Computing for guidance and use of the research computing infrastructure of the Grace high-performance computing cluster. This research used resources of the Advanced Light Source, which is a DOE Office of Science User Facility under Contract No. DE-AC02-05CH11231.

[1] I. Žutić, J. Fabian, and S. D. Sarma, Spintronics: Fundamentals and applications, Rev. Mod. Phys. **76**, 323 (2004).

[2] S. Gardelis, C. G. Smith, C. H. W. Barnes, E. H. Linfield, and D. A. Ritchie, Spin-valve effects in a semiconductor field-effect transistor: A spintronic device, Phys. Rev. B **60**, 7764 (1999).

[3] S. M. Wu, S. A. Cybart, P. Yu, M. D. Rossell, J. X. Zhang, R. Ramesh, and R. C. Dynes, Reversible electric control of exchange bias in a multiferroic field-effect device, Nat. Mater. **9**, 756 (2010).

[4] S. Manipatruni, D. E. Nikonov, C.-C. Lin, T. A. Gosavi, H. Liu, B. Prasad, Y.-L. Huang, E. Bonturim, R. Ramesh *et al.*, Scalable energy-efficient magnetoelectric spin–orbit logic, Nature (London) **565**, 35 (2019).

[5] P. Noël, F. Trier, L. M. Vicente Arche, J. Bréhin, D. C. Vaz, V. Garcia, S. Fusil, A. Barthélémy, L. Vila *et al.*, Non-volatile electric control of spin–charge conversion in a $SrTiO_3$ Rashba system, Nature (London) **580**, 483 (2020).

[6] N. A. Hill, Why are there so few magnetic ferroelectrics? J. Phys. Chem. B **104**, 6694 (2000).

[7] N. A. Spaldin and R. Ramesh, Advances in magnetoelectric multiferroics, Nat. Mater. **18**, 203 (2019).

[8] J. Wang, J. B. Neaton, H. Zheng, V. Nagarajan, S. B. Ogale, B. Liu, D. Viehland, V. Vaithyanathan, D. G. Schlom *et al.*, Epitaxial $BiFeO_3$ multiferroic thin film heterostructures, Science **299**, 1719 (2003).

[9] J. Krempaský, S. Muff, F. Bisti, M. Fanciulli, H. Volfová, A. P. Weber, N. Pilet, P. Warnicke, H. Ebert *et al.*, Entanglement and manipulation of the magnetic and spin–orbit order in multiferroic Rashba semiconductors, Nat. Commun. **7**, 13071 (2016).

[10] H. Przybylińska, G. Springholz, R. T. Lechner, M. Hassan, M. Wegscheider, W. Jantsch, and G. Bauer, Magnetic-field-induced ferroelectric polarization reversal in the multiferroic $Ge_{1-x}Mn_xTe$ semiconductor, Phys. Rev. Lett. **112**, 047202 (2014).

[11] J. A. Mundy, C. M. Brooks, M. E. Holtz, J. A. Moyer, H. Das, A. F. Rébola, J. T. Heron, J. D. Clarkson, S. M. Disseler *et al.*, Atomically engineered ferroic layers yield a room-temperature magnetoelectric multiferroic, Nature (London) **537**, 523 (2016).

[12] S. Valencia, A. Crassous, L. Bocher, V. Garcia, X. Moya, R. O. Cherifi, C. Deranlot, K. Bouzehouane, S. Fusil *et al.*, Interface-induced room-temperature multiferroicity in $BaTiO_3$, Nat. Mater. **10**, 753 (2011).

[13] C. A. F. Vaz, J. Hoffman, C. H. Ahn, and R. Ramesh, Magnetoelectric coupling effects in multiferroic complex oxide composite structures, Adv. Mater. **22**, 2900 (2010).

[14] T. L. Meyer, A. Herklotz, V. Lauter, J. W. Freeland, J. Nichols, E.-J. Guo, S. Lee, T. Z. Ward, N. Balke *et al.*, Enhancing interfacial magnetization with a ferroelectric, Phys. Rev. B **94**, 174432 (2016).

[15] L. Jiang, W. S. Choi, H. Jeen, T. Egami, and H. N. Lee, Strongly coupled phase transition in ferroelectric/correlated electron oxide heterostructures, Appl. Phys. Lett. **101**, 042902 (2012).

[16] V. Garcia, M. Bibes, L. Bocher, S. Valencia, F. Kronast, A. Crassous, X. Moya, S. Enouz-Vedrenne, A. Gloter *et al.*, Ferroelectric control of spin polarization, Science **327**, 1106 (2010).

[17] G. Radaelli, D. Petti, E. Plekhanov, I. Fina, P. Torelli, B. R. Salles, M. Cantoni, C. Rinaldi, D. Gutiérrez *et al.*, Electric control of magnetism at the $Fe/BaTiO_3$ interface, Nat. Commun. **5**, 3404 (2014).

[18] H. L. Meyerheim, F. Klimenta, A. Ernst, K. Mohseni, S. Ostanin, M. Fechner, S. Parihar, I. V. Maznichenko, I. Mertig *et al.*, Structural secrets of multiferroic interfaces, Phys. Rev. Lett. **106**, 087203 (2011).

[19] J. D. Burton and E. Y. Tsymbal, Giant tunneling electroresistance effect driven by an electrically controlled spin valve at a complex oxide interface, Phys. Rev. Lett. **106**, 157203 (2011).

[20] G. Radaelli, D. Gutiérrez, M. Qian, I. Fina, F. Sánchez, L. Baldrati, J. Heidler, C. Piamonteze, R. Bertacco *et al.*, Strain-Controlled Responsiveness of Slave Half-Doped Manganite $La_{0.5}Sr_{0.5}MnO_3$ Layers Inserted in $BaTiO_3$ Ferroelectric Tunnel Junctions, Adv. Electron. Mater. **2**, 1600368 (2016).

[21] A. Ohtomo and H. Y. Hwang, A high-mobility electron gas at the $LaAlO_3/SrTiO_3$ heterointerface, Nature (London) **427**, 423 (2004).

[22] A. Santander-Syro, O. Copie, T. Kondo, F. Fortuna, S. Pailhes, R. Weht, X. Qiu, F. Bertran, A. Nicolaou *et al.*, Two-dimensional electron gas with universal subbands at the surface of $SrTiO_3$, Nature (London) **469**, 189 (2011).

[23] W. Meevasana, P. D. C. King, R. H. He, S. K. Mo, M. Hashimoto, A. Tamai, P. Songsiriritthigul, F. Baumberger, and Z. X. Shen, Creation and control of a two-dimensional electron liquid at the bare $SrTiO_3$ surface, Nat. Mater. **10**, 114 (2011).

[24] H. K. Yoo, L. Moreschini, A. Bostwick, A. L. Walter, T. W. Noh, E. Rotenberg, and Y. J. Chang, Enhanced tunability of two-dimensional electron gas on $SrTiO_3$ through heterostructuring, Curr. Appl. Phys. **20**, 1268 (2020).

[25] T. C. Rödel, F. Fortuna, S. Sengupta, E. Frantzeskakis, P. L. Fèvre, F. Bertran, B. Mercey, S. Matzen, G. Agnus *et al.*, Universal fabrication of 2D electron systems in functional oxides, Adv. Mater. **28**, 1976 (2016).

[26] D. C. Vaz, P. Noël, A. Johansson, B. Göbel, F. Y. Bruno, G. Singh, S. Mckeown-Walker, F. Trier, L. M. Vicente-Arche *et al.*, Mapping spin–charge conversion to the band structure in a topological oxide two-dimensional electron gas, Nat. Mater. **18**, 1187 (2019).

[27] M. Bibes, J. E. Villegas, and A. Barthélémy, Ultrathin oxide films and interfaces for electronics and spintronics, Adv. Phys. **60**, 5 (2011).

[28] J. Bréhin, Y. Chen, M. D'Antuono, S. Varotto, D. Stornaiuolo, C. Piamonteze, J. Varignon, M. Salluzzo, and M. Bibes, Coexistence and coupling of ferroelectricity and magnetism in an oxide two-dimensional electron gas, Nat. Phys. **19**, 823 (2023).

[29] Y. J. Chang, L. Moreschini, A. Bostwick, G. A. Gaines, Y. S. Kim, A. L. Walter, B. Freelon, A. Tebano, K. Horn *et al.*, Layer-by-layer evolution of a two-dimensional electron gas near an oxide interface, Phys. Rev. Lett. **111**, 126401 (2013).

[30] C.-T. Kuo, G. Conti, J. E. Rault, C. M. Schneider, S. Nemšák, and A. X. Gray, Emergent phenomena at oxide interfaces studied with standing-wave photoelectron spectroscopy, J. Vac. Sci. **40**, 020801 (2022).

[31] H. C. Xu, R. Peng, D. W. Shen, and D. L. Feng, In situ engineering and characterization on the artificial heterostructures of correlated materials with integrated OMBE–ARPES, J. Electron. Spectrosc. Relat. Phenom. **200**, 347 (2015).

[32] L. Bocher, A. Gloter, A. Crassous, V. Garcia, K. March, A. Zobelli, S. Valencia, S. Enouz-Vedrenne, X. Moya *et al.*, Atomic and electronic structure of the $BaTiO_3/Fe$ interface in multiferroic tunnel junctions, Nano Lett. **12**, 376 (2012).

[33] See Supplemental Material at http://link.aps.org/supplemental/10.1103/PhysRevB.109.155106 for experimental supplementary figures; methods; details on additional first principles calculations; discussion about core-level photoemission spectroscopic results; and discussion about *c*-axis $BaTiO_3$ lattice constant. The Supplemental Material also contains Refs. [34–51].

[34] L. Dudy, M. Sing, P. Scheiderer, J. D. Denlinger, P. Schütz, J. Gabel, M. Buchwald, C. Schlueter, T. L. Lee *et al.*, In situ control of separate electronic phases on $SrTiO_3$ surfaces by oxygen dosing, Adv. Mater. **28**, 7443 (2016).

[35] Y. J. Shin, J. Jiang, Y. Jia, F. J. Walker, and C. H. Ahn, Low temperature growth of epitaxial ferroelectric $BaTiO_3$, APL Mater. **9**, 041104 (2021).

[36] Z. Wen, X. Qiu, C. Li, C. Zheng, X. Ge, A. Li, and D. Wu, Mechanical switching of ferroelectric polarization in ultrathin $BaTiO_3$ films: The effects of epitaxial strain, Appl. Phys. Lett. **104**, 042907 (2014).

[37] S. Choudhury, Y. L. Li, L. Q. Chen, and Q. X. Jia, Strain effect on coercive field of epitaxial barium titanate thin films, Appl. Phys. Lett. **92**, 142907 (2008).

[38] D. Kan and Y. Shimakawa, Controlled cation stoichiometry in pulsed laser deposition-grown $BaTiO_3$ epitaxial thin films with laser fluence, Appl. Phys. Lett. **99**, 081907 (2011).

[39] P. Giannozzi, S. Baroni, N. Bonini, M. Calandra, R. Car, C. Cavazzoni, D. Ceresoli, G. L. Chiarotti, M. Cococcioni *et al.*, QUANTUM ESPRESSO: A modular and open-source soft-

ware project for quantum simulations of materials, J. Condens. Matter Phys. **21**, 395502 (2009).

[40] V. I. Anisimov, F. Aryasetiawan, and A. I. Lichtenstein, First-principles calculations of the electronic structure and spectra of strongly correlated systems: The LDA+ U method, J. Condens. Matter Phys. **9**, 767 (1997).

[41] M. Fuchs and M. Scheffler, Ab initio pseudopotentials for electronic structure calculations of poly-atomic systems using density-functional theory, Comput. Phys. Commun. **119**, 67 (1999).

[42] S. Moser, An experimentalist's guide to the matrix element in angle resolved photoemission, J. Electron. Spectrosc. Relat. Phenom. **214**, 29 (2017).

[43] G. H. Kwei, A. C. Lawson, S. J. L. Billinge, and S. W. Cheong, Structures of the ferroelectric phases of barium titanate, J. Phys. Chem. **97**, 2368 (1993).

[44] H. J. Monkhorst and J. D. Pack, Special points for Brillouin-zone integrations, Phys. Rev. B **13**, 5188 (1976).

[45] J. P. Perdew and Y. Wang, Accurate and simple analytic representation of the electron-gas correlation energy, Phys. Rev. B **45**, 13244 (1992).

[46] S. L. Dudarev, G. A. Botton, S. Y. Savrasov, C. J. Humphreys, and A. P. Sutton, Electron-energy-loss spectra and the structural stability of nickel oxide: An LSDA+ U study, Phys. Rev. B **57**, 1505 (1998).

[47] L. A. Agapito, A. Ferretti, A. Calzolari, S. Curtarolo, and M. B. Nardelli, Effective and accurate representation of extended Bloch states on finite Hilbert spaces, Phys. Rev. B **88**, 165127 (2013).

[48] L. A. Agapito, S. Ismail-Beigi, S. Curtarolo, M. Fornari, and M. B. Nardelli, Accurate tight-binding Hamiltonian matrices from ab initio calculations: Minimal basis sets, Phys. Rev. B **93**, 035104 (2016).

[49] Y. Zhang, J. Sun, J. P. Perdew, and X. Wu, Comparative first-principles studies of prototypical ferroelectric materials by LDA, GGA, and SCAN meta-GGA, Phys. Rev. B **96**, 035143 (2017).

[50] S. Moser, L. Moreschini, J. Jaćimović, O. S. Barišić, H. Berger, A. Magrez, Y. J. Chang, K. S. Kim, A. Bostwick *et al.*, Tunable polaronic conduction in anatase TiO_2, Phys. Rev. Lett. **110**, 196403 (2013).

[51] P. Lutz, S. Moser, V. Jovic, Y. J. Chang, R. J. Koch, S. Ulstrup, J. S. Oh, L. Moreschini, S. Fatale *et al.*, Volatile two-dimensional electron gas in ultrathin $BaTiO_3$ films, Phys. Rev. Mater. **2**, 094411 (2018).

[52] H. Terauchi, Y. Watanabe, H. Kasatani, K. Kamigaki, Y. Yano, T. Terashima, and Y. Bando, Structural study of epitaxial $BaTiO_3$ crystals, J. Phys. Soc. Jpn. **61**, 2194 (1992).

[53] W. Tian, J. C. Jiang, X. Q. Pan, J. H. Haeni, Y. L. Li, L. Q. Chen, D. G. Schlom, J. B. Neaton, K. M. Rabe *et al.*, Structural evidence for enhanced polarization in a commensurate short-period $BaTiO_3/SrTiO_3$ superlattice, Appl. Phys. Lett. **89**, 092905 (2006).

[54] Y. S. Kim, D. H. Kim, J. D. Kim, Y. J. Chang, T. W. Noh, J. H. Kong, K. Char, Y. D. Park, S. D. Bu *et al.*, Critical thickness of ultrathin ferroelectric $BaTiO_3$ films, Appl. Phys. Lett. **86**, 102907 (2005).

[55] S. Muff, N. Pilet, M. Fanciulli, A. P. Weber, C. Wessler, Z. Ristić, Z. Wang, N. C. Plumb, M. Radović *et al.*, Influence of ferroelectric order on the surface electronic structure of $BaTiO_3$ films studied by photoemission spectroscopy, Phys. Rev. B **98**, 045132 (2018).

[56] D.-C. Zhang and J.-X. Li, Impurity effects on quasiparticle dispersion in a d-wave superconductor, Phys. Rev. B **79**, 064512 (2009).

[57] T. Yamashita and P. Hayes, Analysis of XPS spectra of Fe^{2+} and Fe^{3+} ions in oxide materials, Appl. Surf. Sci. **254**, 2441 (2008).

[58] M. Fechner, I. V. Maznichenko, S. Ostanin, A. Ernst, J. Henk, P. Bruno, and I. Mertig, Magnetic phase transition in two-phase multiferroics predicted from first principles, Phys. Rev. B **78**, 212406 (2008).

[59] C.-G. Duan, S. S. Jaswal, and E. Y. Tsymbal, Predicted magnetoelectric effect in $Fe/BaTiO_3$ multilayers: Ferroelectric control of magnetism, Phys. Rev. Lett. **97**, 047201 (2006).

[60] P. Zhang, P. Richard, T. Qian, Y.-M. Xu, X. Dai, and H. Ding, A precise method for visualizing dispersive features in image plots, Rev. Sci. Instrum. **82**, 043712 (2011).